

AGB winds in interacting binary stars

Luis C. Bermúdez-Bustamante,^{*} G. García-Segura, W. Steffen and L. Sabin

Instituto de Astronomía, Universidad Nacional Autónoma de México, km 107 Carr. Tijuana-Ensenada, Ensenada, B. C., 22860, México

Accepted XXX. Received YYY; in original form ZZZ

ABSTRACT

We perform numerical simulations to investigate the stellar wind from interacting binary stars. Our aim is to find analytical formulae describing the outflow structure. In each binary system the more massive star is in the asymptotic giant branch and its wind is driven by a combination of pulsations in the stellar surface layers and radiation pressure on dust, while the less massive star is in the main sequence. Time averages of density and outflow velocity of the stellar wind are calculated and plotted as profiles against distance from the centre of mass and colatitude angle. We find that mass is lost mainly through the outer Lagrangian point L_2 . The resultant outflow develops into a spiral at low distances from the binary. The outflowing spiral is quickly smoothed out by shocks and becomes an excretion disk at larger distances. This leads to the formation of an outflow structure with an equatorial density excess, which is greater in binaries with smaller orbital separation. The pole-to-equator density ratio reaches a maximum value of $\sim 10^5$ at Roche-Lobe Overflow state. We also find that the gas stream leaving L_2 does not form a circumbinary ring for stellar mass ratios above 0.78, when radiation pressure on dust is taken into account. Analytical formulae are obtained by curve fitting the 2-dimensional, azimuthally averaged density and outflow velocity profiles. The formulae can be used in future studies to setup the initial outflow structure in hydrodynamic simulations of common-envelope evolution and formation of planetary nebulae.

Key words: binaries: close – stars: AGB and post-AGB – stars: winds, outflows –ISM: planetary nebulae

1 INTRODUCTION

Single, low- and intermediate-mass stars lose their envelopes through slow, dense winds at the asymptotic giant branch (AGB) phase. At later stages, the fast and tenuous winds originating from the remnant stars interact with the inner layers of the expanding envelopes. This leads to the formation of planetary nebulae (PNe) once the remnant stars evolve towards higher effective temperatures and ionize the circumstellar gas (Kwok et al. 1978; Kwok 2000). For the case of binary stars with the same mass range, the envelope ejection could be more violent, either at the red giant branch phase or at the AGB phase, if the system goes through a common envelope (CE). In both cases, the envelope ejection determines the distribution of gas in the circumstellar medium.

A fascinating, still unsolved problem of PNe is their morphological diversity, specially the bipolar class, a likely outcome of mass-loss geometry at the tip of the AGB (Balick 1987; Corradi & Schwarz 1995; Manchado et al. 1996; Sahai

et al. 2007). Some numerical computations in the context of the interacting stellar winds model (Kwok 2002) have reproduced a wide diversity of nebular shapes, but they assume arbitrary functions for the density and outflow velocity distribution of the slow AGB wind (Mellema et al. 1991; Icke et al. 1992). A bipolar nebula can be formed if the density of the slow AGB wind increases towards the equatorial plane (Kahn & West 1985; Balick 1987; Icke et al. 1989; Soker & Livio 1989; Dwarkadas et al. 1996; García-Segura et al. 1999; Huarte-Espinosa et al. 2012). What causes this pole-to-equator density ratio in the AGB wind is a matter of discussion, but a stellar companion is the most promising shaping mechanism (García-Segura et al. 2014). In fact, $\sim 40\%$ of the symbiotic stars have bipolar nebulae (Schwarz & Monteiro 2004), and morpho-kinematical models of some PNe show that their symmetry axes are perpendicular to the orbital plane of their binary cores (e.g. Jones et al. 2012). The extremely low probability for this perpendicularity to be a random event (Hillwig et al. 2016), shows a physical link between binary stars and nebular morphology.

Binary nuclei of PNe with orbital separations smaller than the typical radius of their progenitor AGB component

^{*} E-mail: luisb@astro.unam.mx

suggest a loss of mass and angular momentum from the stellar systems in previous evolutionary stages. The basic formation scenario for close binaries begins when the primary star fills its Roche lobe during the ascent towards the AGB phase and transfers mass at dynamical timescales to a main-sequence companion (secondary star). The latter cannot accrete or expel rapidly enough the donated material, from which a CE is formed (Ivanova et al. 2013). Gravitational drag transports orbital energy and angular momentum from the stellar system to the CE and reduces the orbital separation. The envelope is ejected leaving a tight binary star if sufficient energy is transferred, otherwise a stellar merger will occur. The formation of aspherical PNe by CE evolution is not fully understood (García-Segura et al. 2018), given that the details of the ejection mechanisms or their efficiency are unknown (Sabach et al. 2017), and observations of this brief stellar phase (Chamandy et al. 2019) are difficult.

With the current computing power, hydrodynamic simulations of the entire CE phase are not possible, owing to its three-dimensional geometry and the wide range of length and time scales of the physical processes involved (Prust & Chang 2019). In consequence numerical studies placed an emphasis on the dynamical spiral-in phase (Ricker & Taam 2012; Passy et al. 2012). However, initial conditions in computations of CE evolution may affect the outcome, specially when the orbital separation shrinks on dynamical timescales, not giving enough time for dissipation of the density structures formed immediately before. Therefore, a constant-density background gas in pressure equilibrium with the surface of the primary star at the onset of simulations (Ricker & Taam 2012; Staff et al. 2016), or placing the companion star on the surface of the red giant (Ohlmann et al. 2016) may not be realistic situations. In order to improve computations of CE evolution, specially the interaction of the CE ejecta with the previous circumbinary medium, the structure of the gas around the binary system has to be realistically calculated. Thus, the interaction of the AGB wind with the secondary star is very important in this context.

The effects of a stellar companion in the hydrodynamics of the AGB wind were previously investigated by Mastrodomos & Morris (1999); Gawryszczak et al. (2002); Mohamed & Podsiadlowski (2007); Chen et al. (2017), considering only detached binaries. For the above cases, the AGB wind can be simple, well modelled as a supersonic flow, with a constant expansion velocity of the order of 15 km s^{-1} . However, for the case of semi-detached binary stars, the computation of the AGB wind has to be solved from the stellar surface, since the orbit of the binary lies inside the region where the AGB wind is accelerated. Thus, much more physics needs to be included in the modelling, and a more complete knowledge of the AGB wind has to be taken into account. In other words, the form in which the gas is ejected from the stellar surface and is accelerated up to the asymptotic expansion velocity has to be explicitly computed.

Observations of molecular emission lines from AGB stars show that many of them undergo high mass-loss rates through slow, dense winds (De Beck et al. 2010; Wittkowski et al. 2018). Unfortunately, for late-type giant stars, a complete explanation of the mass-loss mechanism is still missing. Consequently, estimations of the mass-loss rates must come from observations. However, it is well known that AGB

winds have asymptotic outflow speeds lower than the stellar surface escape velocity (Ramstedt et al. 2009), in comparison with less evolved Red Giant Branch stars (e.g. Carpenter et al. 2018). This indicates that work is done by the mass-loss mechanisms mostly to overcome the gravitational well of the star, instead of accelerating the wind to its asymptotic speed. Therefore most of the wind driving energy is injected in the subsonic regions of the flow, since the gravitational potential falls off as the inverse of the distance to the centre of the star. Furthermore, the energy must be added in the form of work done by a force rather than in the form of heat, since radiative cooling is very efficient in the inner parts of the dense winds (Holzer & MacGregor 1985; Lamers & Cassinelli 1999).

In addition, mass-loss rates in AGB stars increase with pulsation period, bolometric luminosity and optical depth at infrared wavelengths (Sloan et al. 2010; Danilovich et al. 2015; McDonald et al. 2018). From these results it is thought that AGB winds are driven by a combination of pulsation-induced shock-waves and radiation pressure on dust (Nowotny et al. 2010). These shock-waves eject material into the stellar atmosphere to distances where dust is formed under low temperature and high density conditions. The dust is then accelerated by absorption and scattering of the stellar radiation field and transfers its momentum to the gas through collisions, inducing a slow wind (Höfner & Olofsson 2018). This is basically the scenario that we include in this study.

We perform numerical simulations of the stellar wind in both detached and semi-detached binary stars. Our goal is to obtain analytical formulae describing the density and outflow velocity of the wind, which can be useful in modelling the interaction of the CE ejecta with the surrounding medium and the later formation of bipolar PNe (García-Segura et al. 2018). We focus on the effects of orbital separation and stellar mass ratio on the outflow. To the best of our knowledge, our work is the first attempt to predict the distribution of density and outflow velocity in the stellar wind, based on hydrodynamic models of interacting binaries. In this first article, we obtain 2-dimensional, azimuthally averaged, analytical fits of the outflow structure. Although our simulations are limited by resolution, the qualitative results give an important first insight of such a complex, 3-D problem.

The numerical setup is described in section 2. The effects of orbital parameters and stellar mass ratio q on the outflow structure are described in section 3. Discussions of results are presented in section 4 and conclusions are provided in section 5.

2 METHOD

We study the interaction of an AGB wind with a companion star using 3-dimensional, hydrodynamical simulations. The computations use a nested mesh scheme. We have used stellar pulsations and radiation pressure on dust grains to drive the AGB wind. The details are described in the next subsections.

2.1 The binary system

The binary system consists of an AGB star with a mass of $M_1 = 2.2 M_\odot$ and a secondary star on the main sequence with a mass of $M_2 = 0.8 M_\odot$ (Figure 1). These values are taken from [García-Segura et al. \(2016\)](#). We assume a fundamental-mode pulsation period of $P = 300$ d for our AGB star. This period is within the range of values derived from infrared observations ([Chibueze et al. 2016](#)). With the above values of mass and pulsation period, our AGB star has a radius of $R_1 = 316 R_\odot$ ([Ostlie & Cox 1986](#)). We adopt an orbital separation of $a = 674.3 R_\odot$. This choice for the orbital separation ensures that the secondary star lies in a region where dust is absent in the outflow. Observations show that dust is formed at about two stellar radii ([Norris et al. 2012](#)) from the centre of the AGB star.

According to the Eggleton formula ([Eggleton 1983](#)),

$$\frac{R_{RL}}{a} = \frac{0.49 q_E^{2/3}}{0.6 q_E^{2/3} + \ln(1 + q_E^{1/3})}, \quad (1)$$

with a stellar mass ratio $q_E = M_1/M_2 = 2.75$, the radius of the Roche lobe R_{RL} for the primary star is 0.468 times the orbital separation a . Given that $a = 674.3 R_\odot$, $R_{RL} = 315.6 R_\odot$, the primary fills its Roche lobe ([Paczynski 1971](#)).

The choice of the stellar mass for the primary in [García-Segura et al. \(2016\)](#) was based on the fact that progenitor stars of bipolar PNe seems to be more massive than $2 M_\odot$. This conclusion is supported by the distribution of bipolar PNe towards lower latitudes above the Galactic plane ([Corradi & Schwarz 1995](#)) and their nitrogen enrichment compared to round or elliptical PNe ([Stanghellini et al. 2006](#)). The choice of the stellar mass for the secondary was based on observational studies which show that the mass ratio distribution $q = M_2/M_1$ for nearby binary stars (≤ 100 au) has a maximum close to ~ 0.3 ([Gullikson et al. 2016](#)).

We also increase the mass of the companion to $M_2 = 1.6 M_\odot$, $M_2 = 2 M_\odot$ and $M_2 = 2.2 M_\odot$. These values are chosen to test whether systems with larger mass ratios $q = M_2/M_1$ form gravitationally-bound circumbinary rings ([Shu et al. 1979](#); [Pejcha et al. 2016](#)) when radiation pressure on dust is taken into account.

The binary system is assumed to follow circular orbits, have synchronous rotation and their spin axes are perpendicular to the orbital plane.

2.2 The hydrodynamic code

We use the adaptive-mesh refinement hydrodynamic code WALICXE3D ([Toledo-Roy et al. 2014](#)), which is a 3D extension of the code WALICXE ([Esquivel et al. 2010](#)), to calculate the interaction between the secondary star and the AGB wind. We approximate the stars as point sources of gravity and neglect self-gravity (e.g. [de Val-Borro et al. 2009](#); [Chen et al. 2017](#)).

The physical dimensions of the computational domain, in Cartesian XYZ coordinates, are $9,000 \times 9,000 \times 4,500 R_\odot$ ($41.76 \times 41.76 \times 20.88$ au). This numerical domain consists of three nested meshes fixed to an inertial frame of reference, whose origin coincides with the centre of mass (barycentre) of the system. We prefer to use a nested mesh to concentrate the highest resolution always at the centre of the domain,

instead of using the adaptive mesh refinement algorithm. Each mesh has $128 \times 128 \times 64$ cubical cells, where the shortest dimension Z is perpendicular to the orbital plane (XY plane), and each of them is a factor 2 smaller in each axis compared to the next coarser mesh. The formal resolution limit in grid-based codes is set by the Nyquist wavelength, which is the lowest wavelength for a wave to reliably propagate across the grid. The Nyquist wavelength is equal to twice the smallest space interval on the grid ([Bodenheimer et al. 2007](#)). Based on this, the resolution in our simulations is $\sim 35.2 R_\odot$, which corresponds to twice the size of each cell in the innermost mesh ($\sim 17.6 R_\odot$). The orbital plane has a reflective boundary condition, while the other boundaries have free-outflowing conditions.

We consider an ideal gas composed of neutral atoms and assume that the hydrogen to helium number ratio is 10 to 1. Therefore the gas has a ratio of specific heats $\gamma = 5/3$ and a constant mean molecular weight per particle $\mu = 1.27$. The radiative cooling is given by vibrational transitions of CO molecules ([Gail & Sedlmayr 2013](#), Appendix 3) and collisional excitation and ionization of hydrogen ([Black 1981](#)), using the first-order implicit scheme described in [Townsend \(2009\)](#).

2.3 Numerical approach for the primary star

For simplifying the hydrodynamic models, we assume a spherical AGB star (i.e. the surface of the primary star is not an equipotential surface). As an initial condition, the slow wind is setup spherically symmetric with respect to the centre of the AGB star and follows a velocity law of the form ([Lamers & Cassinelli 1999](#), chap. 2)

$$v(r_1) = v_0 + (v_\infty - v_0)(1 - R_1/r_1)^\beta, \quad (2)$$

where $v(r_1)$ is the wind velocity at a distance r_1 from the centre of the AGB star, whose radius is R_1 . The parameter β describes the acceleration in the inner regions of the wind. In cool giant stars the wind accelerates more slowly, corresponding to values of $\beta \geq 1$. We take $\beta = 2.0$ but larger values have been used in literature ([Khoury et al. 2014](#); [Danilovich et al. 2015](#), see also e.g. [Rau et al. 2018](#), for warmer giant stars). The outflow velocity in AGB stars is typically 5 to 25 km s^{-1} ([Ramstedt et al. 2009](#)), for this reason we assign a terminal velocity of $v_\infty = 10 \text{ km s}^{-1}$ and assume that the gas escapes from the stellar surface with a velocity $v_0 = 0.1 \text{ km s}^{-1}$. Higher values of the surface velocity are computed in section 3.2. The initial density of the background gas is obtained using both the velocity field described in equation 2 and the initial mass-loss rate \dot{M} of the AGB star in the continuity equation. The [Vassiliadis & Wood \(1993\)](#) parametrization

$$\log \dot{M}(M_\odot \text{ yr}^{-1}) = -11.4 + 0.0123 P \text{ (days)} \quad (3)$$

gives $\dot{M} \sim 2 \times 10^{-8} M_\odot \text{ yr}^{-1}$, for the adopted period of pulsation $P = 300$ d.

The initial temperature field of the gas T_{eq} at a distance

r_1 and r_2 from the centre of the primary and secondary star, respectively, is (Djurasevic 1986)

$$T_{\text{eq}} = \left(\frac{1}{2}\right)^{\frac{1}{4}} \left(\left[1 - \sqrt{1 - \left(\frac{R_1}{r_1}\right)^2} \right] T_1^4 + \left[1 - \sqrt{1 - \left(\frac{r_s}{r_2}\right)^2} \right] T_s^4 \right)^{\frac{1}{4}}, \quad k_{\text{D}} = \frac{k_{\text{max}}}{1 + e^{(T_{\text{eq}} - T_{\text{cond}})/\xi}}, \quad (10)$$

We assume an effective temperature of $T_1 = 3000$ K for the AGB star. This is a common temperature for Mira variable stars pulsating in their fundamental mode (van Belle et al. 2002).

We adopt an effective temperature $T_s = 5000$ K and a stellar radius $r_s = 1 R_{\odot}$ for our secondary star of mass $M_2 = 0.8 M_{\odot}$, following the temperature-mass and mass-radius diagrams from Torres et al. (2010).

The wind from the AGB is driven by stellar pulsations coupled with radiation pressure on dust grains. Simple harmonic variations of the gas velocity $V(t)$ at the position $R(t)$ are employed to model the pulsations as follows

$$V(t) = \Delta u \cos(2\pi t/P), \quad (5)$$

$$R(t) = R_0 + \frac{\Delta u}{2\pi/P} \sin(2\pi t/P), \quad (6)$$

We assume an initial position of pulsation of $R_0 = 0.9 R_1$. This value is chosen because pulsations in AGB stars are believed to be driven in the hydrogen-ionization zone, located approximately at $0.1 - 0.2 R_1$ below the photosphere (Berlitz-Arthaud 2003; Fadeyev 2016). $\Delta u = 5 \text{ km s}^{-1}$ and $P = 300$ d are the constant velocity amplitude and period of the pulsations, respectively. The former value is chosen from the range of radial velocities in AGB stars derived from observed Doppler-shifts of spectral lines (Lebzelter & Hinkle 2002; Nowotny et al. 2010).

From the equations of equilibrium (Applegate 1988; Chandrasekhar 1967, chap. 9), the temperature and density structure of the AGB surface layers are given by

$$T(r_1) = T_1 + \frac{1.79}{2.18} \frac{GM_1 \mu m_{\text{H}}}{k_{\text{B}}} \left(\frac{1}{r_1} - \frac{1}{R_1} \right), \quad (7)$$

$$\rho(r) = \left[\left(\frac{1.79}{2.18} \right) \left(\frac{16\pi GM_1 a c \mu m_{\text{H}}}{3k_{\text{B}} L_1 \kappa} \right) \right] T^3(r_1), \quad (8)$$

where k_{B} , G , m_{H} , a , c and L_1 are the Boltzmann constant, the gravitational constant, the atomic mass unit, the radiation constant, the speed of light and the AGB star luminosity, respectively. Note that the law of opacity κ is given by the negative hydrogen ion H^- (Iben 2013, chap. 7). Although we have the AGB stellar structure from García-Segura et al. (2016), it is preferable in our case to use the analytical expressions as in equations 7 and 8, since the grid resolution is limited, and the interpolation produces more numerical errors than the analytical formulae. The remaining AGB interior is assumed to be homogeneous and isothermal.

We have considered the AGB star as a point source of radiation, thus the radiative acceleration takes the form:

$$a_{\text{rad}} = \frac{k_{\text{D}} L_1}{4\pi r^2 c} e_r, \quad (9)$$

where e_r is the unit radial vector and k_{D} is the dust opacity, which is approximated as (Bowen 1988)

$$k_{\text{D}} = \frac{k_{\text{max}}}{1 + e^{(T_{\text{eq}} - T_{\text{cond}})/\xi}}, \quad (10)$$

$T_{\text{cond}} = 1500$ K is the condensation temperature and its range spreads over $\xi = 200$ K. These values are selected because the most abundant dust species in carbon-rich stars, namely amorphous carbon and silicon carbide (Rau et al. 2015), have condensation temperatures between 1300 and 1700 K, approximately (Lodders & Fegley 1995; Leisenring et al. 2008). The parameter k_{max} , which is the maximum value of dust opacity, is a constant adjusted to give slow wind expansion velocities of $\sim 10 - 20 \text{ km s}^{-1}$ towards the pole. The AGB luminosity L_1 is calculated from the stellar effective temperature, radius and pulsation properties

$$L_1 = \pi a c T_1^4 \left(R_1 + \frac{\Delta u}{2\pi/P} \sin(2\pi t/P) \right)^2, \quad (11)$$

2.4 Numerical approach for the secondary star

In our simulations the secondary star is not resolved; it is a point source, since its radius (equal to one solar radius) is smaller than a grid cell of our computational mesh. Therefore, its gravitational potential would induce extremely large accelerations to the nearby gas and, consequently, infinitesimal time-steps. For avoiding this, we smoothed the potential following Ruffert (1993)

$$\phi(r_2) = \frac{-GM_2}{\sqrt{r_2^2 + \varepsilon^2 \delta^2 e^{-(r_2/\varepsilon\delta)^2}}}, \quad (12)$$

The smoothing length δ is equal to the size of one cell in the innermost mesh and r_2 is the distance to the secondary star of mass M_2 . Following Staff et al. (2016) the parameter ε is equal to 3, which ensures a finite gravitational potential at the secondary star position. With this value for ε , the smoothed potential is identical to the true potential at ~ 7 cell widths from the secondary star (see discussion).

Lower values for ε produce similar results at the cost of smaller time-steps, which increases the total computational time.

3 RESULTS

3.1 3-D numerical results

The simulations are first run during a couple of orbits until they reached a steady-state configuration. After that, we calculate 40 orbital cycles to make a time average of the density and outflow velocity of the stellar wind, in order to obtain an axisymmetric, 2-dimensional structure.

Table 1 shows different input parameters such as orbital separation a , mass of the stellar components M_1 and M_2 , mass ratio q , orbital period P_{orb} and maximum dust opacity k_{max} for each binary system. The Model 1 (our fiducial model) is shown in the first line.

The computed mass-loss rates of each model are shown in Table 2. The mass-loss rates are calculated through a

spherical surface of radius $4300 R_{\odot}$ (20.0 au), close to the outer boundaries of the simulation, where the out-flowing material is supersonic.

Figure 2 shows a density snapshot of Model 1 at the orbital plane (XY plane) and Figure 3 shows its time-averaged density (top panel) and outflow velocity (bottom panel) perpendicular to the XZ plane. We find that mass loss in the binary star occurs mainly through the outer Lagrangian point L_2 . The resultant outflow develops into a spiral at low distances from the binary, that is quickly smoothed out by shocks and becomes an excretion disk at larger distances from the stars. This leads to the formation of an outflow structure with an equatorial density enhancement, i.e., with a large pole-to-equator density ratio, as also shown in Chen et al. (2017).

Figure 4 shows the time-averaged density (top panel) and outflow velocity (bottom panel) profiles, as functions of the coordinate X. The coordinate X indicates the distance from the centre of mass. These profiles are obtained at the equatorial plane to study mass-loss sensitivity to orbital separation. Far from the barycentre, the gravitational potential of the binary system approximates that of a single star. Consequently, at distances larger than ~ 8 au the outflow in these models follows similar power-law density and velocity distributions (see subsection 3.2).

Figure 5 shows the time-averaged density (top panel) and outflow velocity (bottom panel) profiles, as functions of the colatitude angle. These profiles are obtained at equidistant points from the barycentre of the system, in the outermost mesh. This figure shows the pole-to-equator density ratio, which reaches a maximum value of $\sim 10^5$ at Roche-Lobe Overflow (RLOF) state for Model 1. The colatitude angle goes from 0° at the pole to 90° at the XY plane (Figure 1).

Models 1, 2 and 3 have equal stellar masses but different orbital periods and separations. When the orbital separation is smaller, the outflow structure changes in the following ways. First, at distances from the centre of mass greater than ~ 4 au, the circumbinary gas is denser in Model 1 with respect to Models 2 and 3 at the orbital plane, as shown in the top panel of Figure 4. This is caused by a larger mass-loss rate from the binary system through the outer Lagrangian points. Second, a stronger deviation from spherical symmetry in the mass-loss geometry is produced, or in other words, the pole-to-equator density ratio increases up to $\sim 10^5$, as it is shown in the top panels of Figure 3 and 5. This is caused by a stronger gravitational focusing of the winds towards the companion star. Third, the outflow is faster (bottom panels of Figure 4 and 5). This is a consequence of the momentum imparted to the wind by the secondary star with a faster orbital motion. The above results give rise to an increase of the mass-loss rate (Table 2).

Models 4, 5 and 6 have equal orbital separation but different companion stellar mass. This produces the following changes in the outflow structure when the mass ratio $q = M_2/M_1$ increases towards unity. First, more material is lost through the outer Lagrangian points and less gas reaches the distant polar regions, as a consequence the pole-to-equator density ratio also increases (top panel of Figure 6). Second, the mass-loss rate is enhanced, as can be seen in Table 2. If both the companion stellar mass and the max-

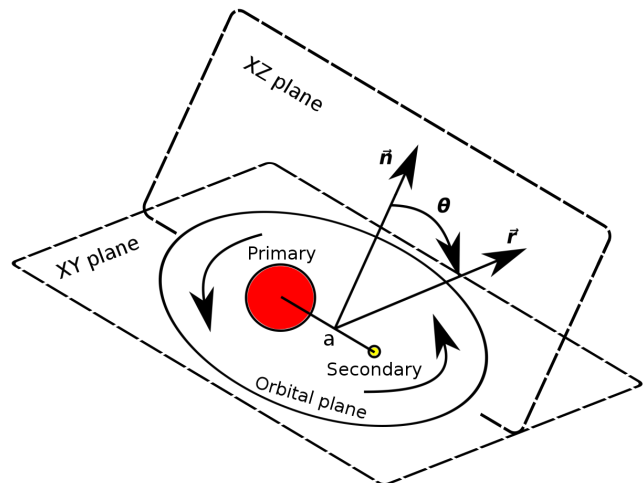


Figure 1. Colatitude angle θ between the position vector \vec{r} of each mesh cell and the unit normal vector \vec{n} to the orbital plane. The orbital separation a is indicated by the line segment joining the stars.

imum dust opacity k_{\max} increase, then the outflow velocity also increases as shown in the bottom panel of Figure 6.

Beyond ~ 10 au from the barycentre, the time-averaged outflow velocity at the orbital plane of Models 4, 5 and 6 becomes larger than the escape velocity relative to the barycentre, as shown in Figure 7. In Models 4, 5 and 6 the stellar mass ratios are equal to 0.73, 0.91 and 1, respectively. Therefore if radiation pressure on dust is included, the gas ejected through the Lagrangian L_2 point does not form an outer ring of gravitationally bound material when $q = M_2/M_1 = 0.73$ (Figure 8) or when $q = M_2/M_1 > 0.78$, as seen in Figures 9 and 10.

For comparison, we have made an adiabatic model (Table 1) without radiative cooling. In this model, the gas behind the pulsation-induced shock can no longer radiate its internal energy and expands adiabatically before the next shock appears. As a consequence, the gas velocity increases. Because of that, the gravitational focusing of the AGB wind towards the orbital plane is underestimated (Gawryszczak et al. 2002) since there is a larger thermal pressure that works against gas compression.

3.2 Analytical fits

Finally, we make a curve fitting to the profiles to find analytical expressions of the outflow structure. The variation with θ of density and outflow velocity in the stellar wind is described using several Gaussian functions in equations 13 and 14, respectively. In these equations, density and outflow velocity are given by the coefficient s near the symmetry axis and by b_i at colatitude angle c_i . The coefficient d_i represents the width of the Gaussian functions. Table 3 shows numerical values of the coefficients for our Models. Density (g cm^{-3}) and outflow velocity (km s^{-1}) as functions of both distance r (in au) from the barycentre and colatitude angle θ (in degrees) are given in equations 15 and 16, respectively. In the former equation the dependence on distance is fitted to a power-law function $\rho \propto r^{-f}$. While in the latter

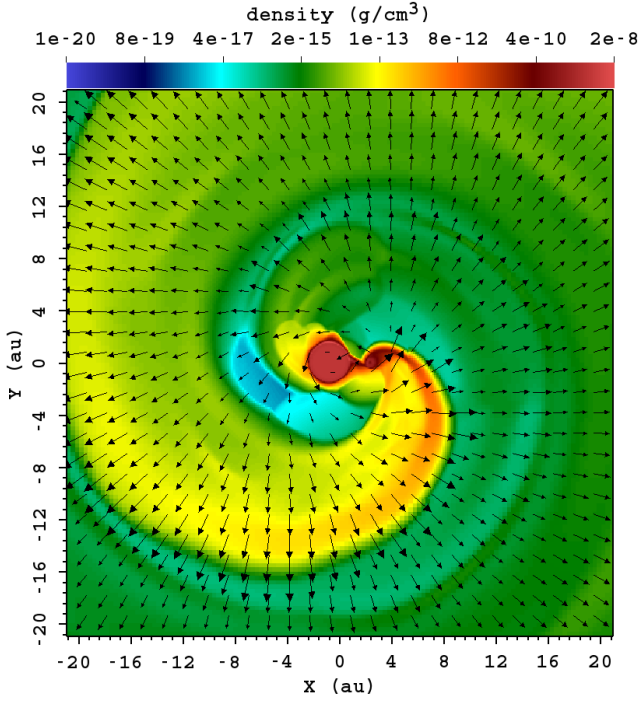


Figure 2. Density map in logarithmic scale at the XY plane for our fiducial model (Model 1). Black arrows represent the velocity field. The centre of mass (barycentre) is located at (0, 0).

equation, we use a velocity field similar to that described in equation 2; however we replace the constant surface velocity v_0 by equation 14.

$$\Psi(\theta) = s + \sum_{i=1}^5 b_i e^{-(\theta - c_i)^2 / d_i^2}, \quad (13)$$

$$\vartheta(\theta) = s + \sum_{i=1}^5 b_i e^{-(\theta - c_i)^2 / d_i^2}, \quad (14)$$

$$\frac{\rho(r, \theta)}{\rho_{\text{ref}}} = \Psi(\theta) \left(\frac{r_c}{r} \right)^f, \quad (15)$$

$$\frac{v(r, \theta)}{V_{\text{orb}}} = \vartheta(\theta) + (\vartheta(\theta) - v_{\infty}) * \left(\frac{r_c}{r} - 1 \right)^f, \quad (16)$$

Given that these expressions could be used as initial conditions characterizing the circumbinary medium in simulations of aspherical PNe at larger spatial dimensions, we choose the length scale parameter r_c as far from the binary star as possible, in a region where the outflow is unbound and its morphology has not changed considerably as compared to inner regions. Taking the above into account, $r_c = 20.0$ au. The parameter v_{∞} is the wind terminal velocity resulting from the simulations. $V_{\text{orb}} = (2\pi a) / P_{\text{orb}}$ and $\rho_{\text{ref}} = \dot{M} / (4\pi r_c^2 V_{\text{orb}})$ are, respectively, velocity and density scale factors. The orbital separation a and the orbital period P_{orb} for each model are given in Table 1, while the total mass-loss rates \dot{M} are shown in Table 2.

Figure 11 and Figures A1 to A6 in the appendix show the analytical fit to the time-averaged density and outflow

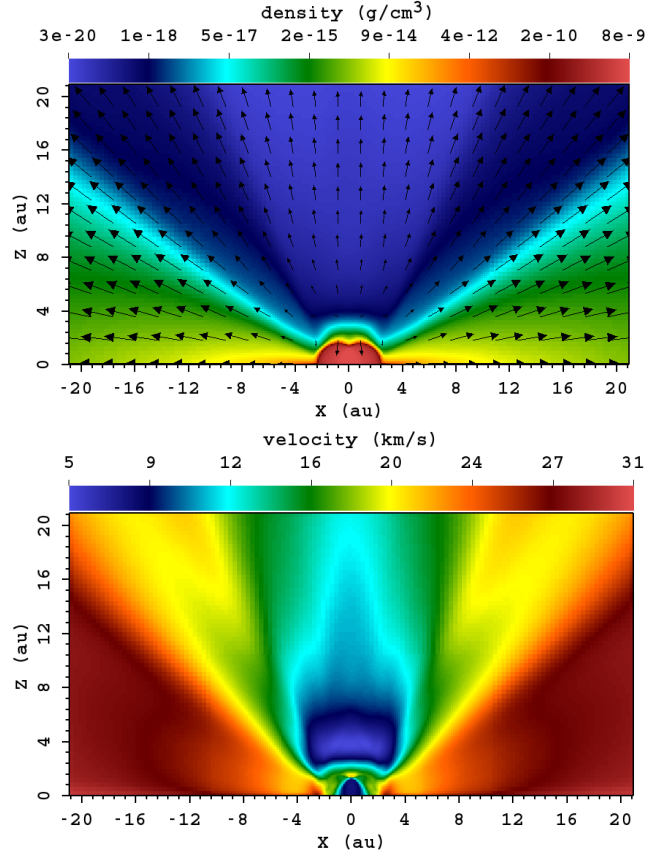


Figure 3. Time-averaged density (top) and outflow velocity (bottom) maps in logarithmic and linear scale, respectively, for our fiducial model at the XZ plane. Black arrows represent the velocity field.

velocity profiles, as functions of the colatitude angle, for our models using equations (13) and (14), respectively.

Finally, Table 4 shows the time-averaged density and outflow velocity of the stellar wind of additional models. For each of these models the initial wind velocity v_0 at the surface of the AGB star is different, while the input parameters such as orbital separation, stellar masses and maximum dust opacity are equal to those in our Model 1 (Table 1). Values for density and outflow velocity were taken at a fixed distance of 20.0 au from the barycentre and at different colatitude angles θ . As can be seen in Table 4, the outflow hydrodynamical structure is not modified considerably with different values for v_0 .

4 DISCUSSION

One of the most important feature from the above results is that the outflow has a complex structure. Our results show that the time-averaged density is maximal at the orbital plane and minimal along the poles. Thus for example, the interactions of an ejected CE will be affected by this gas distribution, even more the subsequent PNe formation (García-Segura et al. 2018). This suggests that the connection between PNe symmetry axis and binary star parameters

Table 1. Input parameters for the binary models.

Models	a (R_{\odot})	M_1 (M_{\odot})	M_2 (M_{\odot})	$q = M_2/M_1$	P_{orb} (yr)	k_{max}	Remarks
1	674.3	2.2	0.8	0.36	3.2	5.6	Fiducial model in RLOF
2	809.2	2.2	0.8	0.36	4.2	5.6	
3	944.0	2.2	0.8	0.36	5.3	5.6	
4	944.0	2.2	1.6	0.73	4.7	6.6	
5	944.0	2.2	2.0	0.91	4.5	8.5	
6	944.0	2.2	2.2	1.0	4.4	8.8	
7	674.3	2.2	0.8	0.36	3.2	5.6	Adiabatic simulation

Table 2. Mass-loss rates for the binary models resulting from our calculations.

Models	\dot{M} ($M_{\odot}\text{yr}^{-1}$)
1	5.8e-5
2	1.6e-6
3	1.2e-7
4	4.4e-6
5	1.8e-5
6	3.2e-5
7	7.2e-4

Table 3. Coefficients for the analytical fits of the outflow structure

Function	s	b_1	c_1	d_1	b_2	c_2	d_2	b_3	c_3	d_3	b_4	c_4	d_4	b_5	c_5	d_5	f
$\rho_1(r, \theta)$	2.9e-5	5.4e-4	39	8.2	8e-4	49	7	1.1	72	7.9	3.5	80.5	6.5	11.6	90	6.2	2.55
$v_1(r, \theta)$	0.42	5.9e-2	13.3	7.8	0.2	30.4	11.4	0.21	57.8	13.3	0	0	0	0.54	90	37.3	1
$\rho_2(r, \theta)$	1.5e-3	4.1e-4	0	6	7.1e-3	42.5	10.5	8.8e-3	58.5	9	1.48	74.5	7.9	10.7	90	10.2	2.55
$v_2(r, \theta)$	0.42	5.2e-2	11.4	6.5	0.16	28.1	13	0.25	54.3	15.5	0.23	68.2	11.1	0.58	90	18.6	1
$\rho_3(r, \theta)$	2.2e-2	5.1e-3	27	7	9.2e-2	49	14.5	0.15	67	10	3.7	79	8	10.1	90	7	2.5
$v_3(r, \theta)$	0.47	7.7e-2	26.1	16.1	0	0	0	0	0	0	0.2	66.2	14.4	0.57	90	17.9	1
$\rho_4(r, \theta)$	5e-4	3.2e-4	0	8	5.1e-4	35	22	1.8e-3	58	8.3	0.62	71.6	6.4	10.8	90	10.9	2.45
$v_4(r, \theta)$	0.24	0.16	22.4	19.9	0	0	0	0.67	66.5	27.2	8.2e-2	78.1	6.4	0.5	90	8.2	1
$\rho_5(r, \theta)$	9.5e-5	0	0	0	4.3e-5	30	15.9	1.2e-4	50	8.9	0.63	72.1	6.9	11.2	90	9.5	2.6
$v_5(r, \theta)$	0.54	0	0	0	6.9e-2	29	14.5	0.41	64.5	20	0.18	80	9.5	0.45	90	7.5	1
$\rho_6(r, \theta)$	3.2e-5	9.9e-6	17	10	0	0	0	3.6e-5	51	8	0.66	72	7	12.1	90	9.3	2.45
$v_6(r, \theta)$	0.52	0	0	0	6.7e-2	34	16.2	0.19	55.7	14	0.46	83.2	26.1	0.19	90	5.6	1
$\rho_7(r, \theta)$	0.2	2.9e-2	20	15	0	0	0	0.33	60	20	0.43	71	10	9.4	90	10.5	2.1
$v_7(r, \theta)$	0.7	1.7e-2	0	7	9.2e-2	39	16	0	0	0	6.7e-2	65	17	0.27	90	12	1

Table 4. Density and outflow velocity of the stellar wind for models with different initial wind velocities at the surface of the AGB star.

Colatitude angle θ	Model with $v_0 = 0.1 \text{ km s}^{-1}$		Model with $v_0 = 1.0 \text{ km s}^{-1}$		Model with $v_0 = 5.0 \text{ km s}^{-1}$	
	ρ (g cm^{-3})	v (km s^{-1})	ρ (g cm^{-3})	v (km s^{-1})	ρ (g cm^{-3})	v (km s^{-1})
5.2	4.5e-20	10.9	4.4e-20	10.9	4.2e-20	11.0
14.5	4.3e-20	15.3	4.2e-20	15.4	3.8e-20	15.5
24.5	6.1e-20	18.1	6.1e-20	18.1	5.7e-20	18.3
34.8	4.1e-19	19.0	4.1e-19	19.0	4.0e-19	19.2
45	2.0e-18	17.9	2.0e-18	17.9	1.9e-18	18.1
55.2	2.9e-17	23.8	2.9e-17	23.8	2.9e-17	23.8
64.7	1.3e-15	26.8	1.3e-15	26.8	1.3e-15	26.8
75.6	2.5e-14	28.7	2.5e-14	28.7	2.5e-14	28.7
85.1	8.0e-14	29.1	8.0e-14	29.1	8.0e-14	29.2

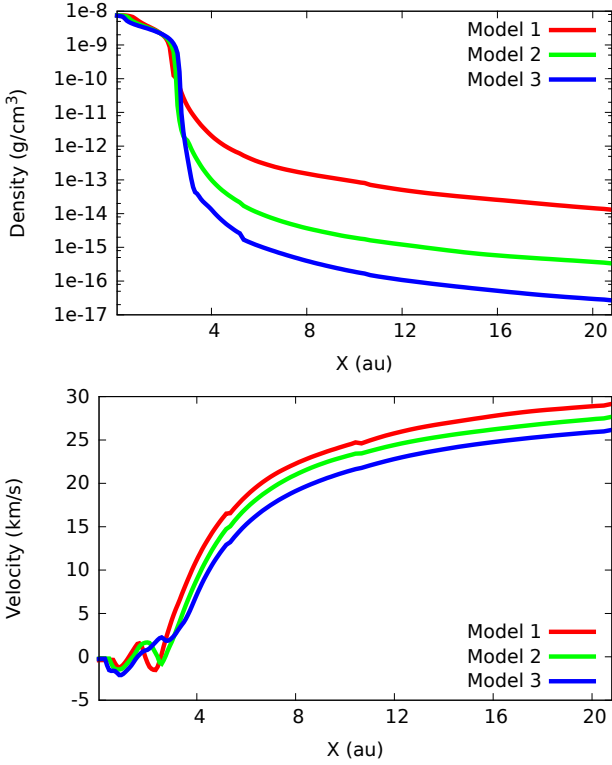


Figure 4. Time-averaged density (top) and outflow velocity (bottom). The horizontal axes indicate the distance from the centre of the mass.

(Jones et al. 2012) is established before RLOF and survives the CE phase.

The pole-to-equator density ratio is also important in the shaping of a hot bubble resulting from the shocked material by a jet from the secondary star, at the RLOF phase (Shiber et al. 2019, and references therein). For the above reasons, the density ratio has to be taken into account to study the correct hydrodynamical evolution of the binary system.

For a single AGB star with pulsation period $P = 300$ days, parametrizations for mass-loss rates from Vassiliadis & Wood (1993); De Beck et al. (2010) agree within one order of magnitude with the mass-loss rate of Model 3, where the binary star has its largest orbital separation and the companion star has the lowest influence. For the other models, the mass-loss rates are larger and comparable to those in AGB stars undergoing superwinds (Renzini 1981; Vassiliadis & Wood 1993).

There are three implications for the above result. First, the AGB timescale could be shortened if such mass-loss rates are maintained or enhanced by the CE (see e.g. De Marco et al. 2011). Second, superwinds at the tip of the AGB phase could be actually gravity-enhanced winds in binary systems approaching RLOF (see e.g. Decin et al. 2019). Third, the stellar evolution of the primary could be driven by the presence of a companion star rather than by intrinsic properties (see e.g. Sana et al. 2012). This can reduce the final mass of white dwarfs in binary systems.

Dynamical interactions between circumbinary disks and binary stars are considered by Artymowicz et al. (1991);

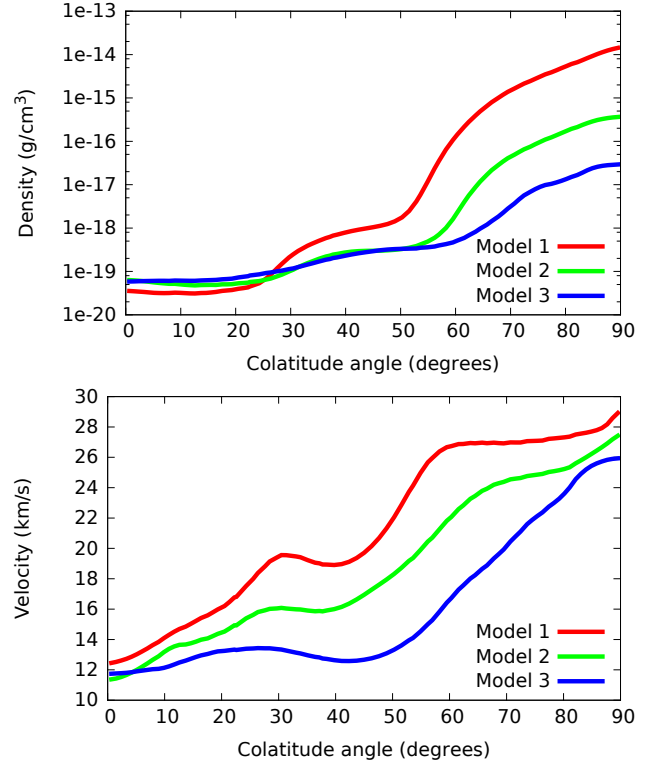


Figure 5. Time-averaged density (top) and outflow velocity (bottom) at 20.0 au from the barycentre of the system for Models 1, 2 and 3. The horizontal axes indicate the colatitude angle which goes from 0° at the pole to 90° at the XY plane.

Dermeine et al. (2013) as a mechanism to increase the orbit eccentricity. However our models show that there is no gravitationally-bounded circumbinary disks when radiation pressure on dust is taken into account. This implies that the above-mentioned mechanism may not work for AGB binaries with dusty winds and approaching RLOF. Our models also suggest that such disks observed in post-AGB binaries (Van Winckel et al. 2006) must be formed after RLOF or when the dust-driven wind is over.

The accretion disk around the main-sequence companion and the Roche lobe of the latter has approximately the same radius (Paczynski 1977). Using equation (1) with the stellar mass ratio $q = M_2/M_1 = 0.8 M_\odot/2.2 M_\odot$ and $a = 674.3 R_\odot$, the Roche lobe radius for the secondary star is $\sim 200 R_\odot$, which is ~ 11 times the size of a mesh cell. At this distance the smoothed gravitational potential is identical to the Newtonian potential, and mass loss through the Lagrangian point L_2 is unaffected. In addition, our simulations of binary systems with the same orbital separation but more massive secondary stars (with a deeper gravitational potential well) show that the outflow structure is well described by the same formulae. Therefore we expect that our qualitative results remain valid, even though the accretion disk physics is not resolved.

Finally, our models show outflows with pole-to-equator density ratios from 10^2 up to $\sim 10^5$, however these values are reduced if radiative cooling is absent. This implies that a complete computation of PNe formation and evolution must include a self-consistent treatment of radiative cooling.

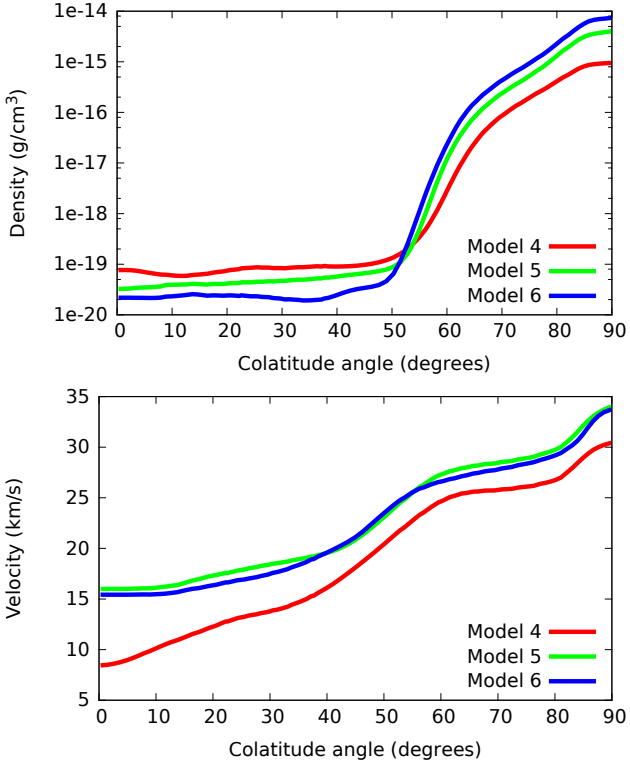


Figure 6. Same as Fig. 5 for models 4, 5 and 6.

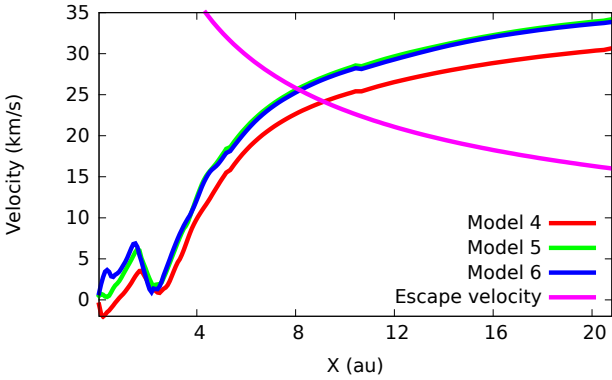


Figure 7. Time-averaged outflow velocity, as function of the X coordinate, for Models 4, 5 and 6. Also shown the escape velocity relative to the barycentre.

The time-averaged structure of the outflows from our interacting binary stars is well described using the proposed analytical formulae. Motivated by the fact that our models include both semi-detached and detached binaries, a future work will explore if our formulae remain valid for a much larger combination of orbital separations and stellar mass ratios.

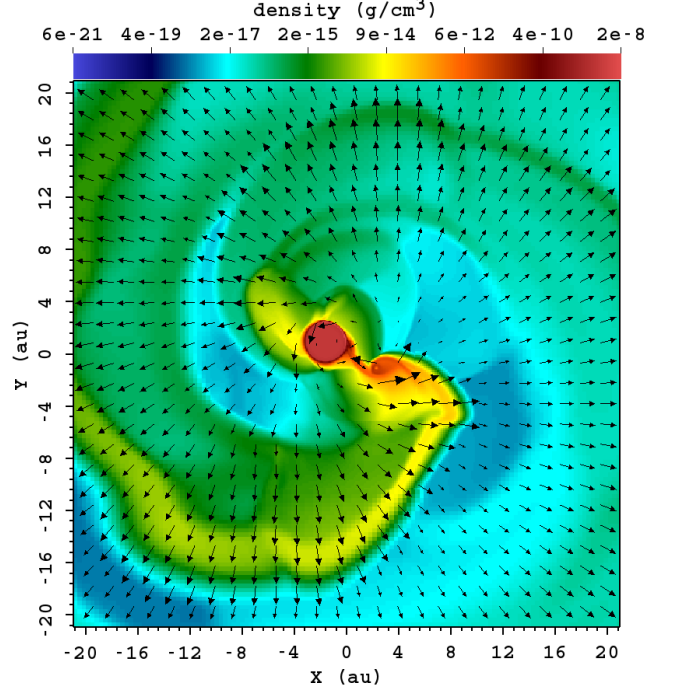


Figure 8. Density map in logarithmic scale at the XY plane for Model 4. Black arrows represent the velocity field. The barycentre is located at (0, 0).

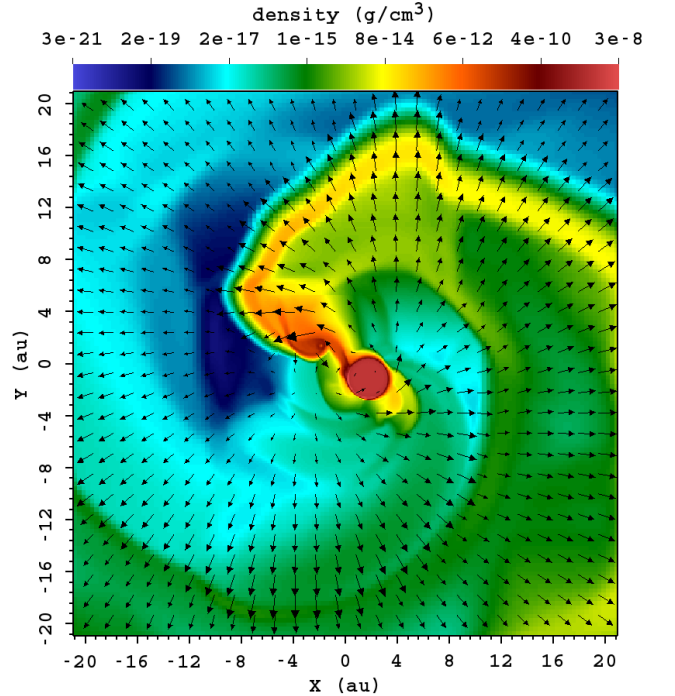


Figure 9. Same as Fig. 8 for Model 5.

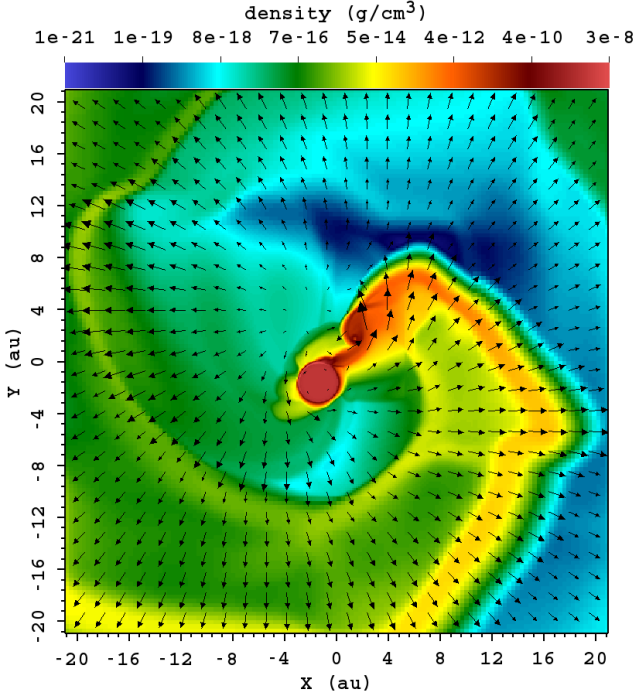


Figure 10. Same as Fig. 8 for Model 6.

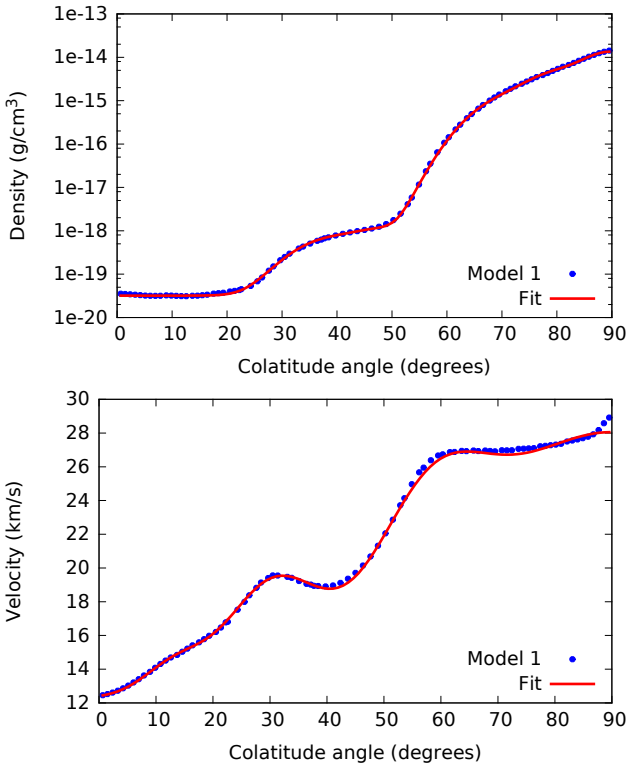


Figure 11. Time-averaged density (top) and outflow velocity (bottom) profiles, as functions of the colatitude angle, at 20.0 au from the barycentre of the system for our fiducial model (• symbols). Solid lines are analytical fits from equations (13) and (14).

5 CONCLUSIONS

We have computed numerically the outflow from interacting binary stars. The results of our study can be summarized as follows: mass loss from an interacting binary system hosting an AGB star is produced mainly through the outer Lagrangian points, as shown also in [Soker & Livio \(1989\)](#); [Mastrodomos & Morris \(1999\)](#); [Mohamed & Podsiadlowski \(2007\)](#).

The resultant pole-to-equator density ratios and mass-loss rates increase in binary systems with smaller orbital separations or with larger mass ratios $q = M_2/M_1$ (top panels of Figures 5 and 6). At the RLOF phase, both density ratio and mass-loss rate have the largest values.

These results agree with the hypothesis of binary stars as a shaping mechanisms of aspherical PNe.

If radiation pressure on dust grains is included, the gas leaving the Lagrangian L_2 point does not establish an outer ring of gravitationally bound matter when $q = M_2/M_1 > 0.78$. This behaviour is the opposite when radiation pressure is not included ([Shu et al. 1979](#); [Pejcha et al. 2016](#); [Chen et al. 2017](#)).

We find analytical formulae describing the outflow structure in terms of distance from the barycentre and the colatitude angle. The formulae can be used in future studies to setup hydrodynamic simulations of CE evolution and the formation of planetary nebulae.

ACKNOWLEDGEMENTS

We thank the anonymous referee for her/his valuable comments, which have improved considerably the article. We thank W. J. Schuster for improving the English of our paper. We thank J. A. Esquivel and J. C. Toledo for making their code available. This work is supported by CONACyT grant 512173, 178253 and DGAPA-PAPIIT 104017. *Software credit*: VISIT ([Childs et al. 2012](#)).

REFERENCES

- Applegate J. H., 1988, *ApJ*, **329**, 803
 Artymowicz P., Clarke C. J., Lubow S. H., Pringle J. E., 1991, *ApJ*, **370**, L35
 Balick B., 1987, *AJ*, **94**, 671
 Berlioz-Arthaud P., 2003, *A&A*, **397**, 943
 Black J. H., 1981, *MNRAS*, **197**, 553
 Bodenheimer P., Laughlin G. P., RÅszycza M., Yorke H. W., 2007, in *Numerical Methods in Astrophysics: An Introduction*. Part of the Series in Astronomy and Astrophysics. Edited by Peter Bodenheimer.
 Bowen G. H., 1988, *ApJ*, **329**, 299
 Carpenter K. G., Nielsen K. E., Kober G. V., Ayres T. R., Wahlgren G. M., Rau G., 2018, *ApJ*, **869**, 157
 Chamandy L., Tu Y., Blackman E. G., Carroll-Nellenback J., Frank A., Liu B., Nordhaus J., 2019, *MNRAS*, **486**, 1070
 Chandrasekhar S., 1967, *An introduction to the study of stellar structure*
 Chen Z., Frank A., Blackman E. G., Nordhaus J., Carroll-Nellenback J., 2017, *MNRAS*, **468**, 4465
 Chibueze J. O., Miyahara T., Omodaka T., Ohta T., Fujii T., Tanaka M., Motohara K., Makoto M., 2016, *ApJ*, **817**, 115
 Childs H., et al., 2012, in *High Performance Visualization—Enabling Extreme-Scale Scientific Insight*. pp 357–372

- Corradi R. L. M., Schwarz H. E., 1995, *A&A*, **293**, 871
- Danilovich T., et al., 2015, *A&A*, **581**, A60
- De Beck E., Decin L., de Koter A., Justtanont K., Verhoelst T., Kemper F., Menten K. M., 2010, *A&A*, **523**, A18
- De Marco O., Passy J.-C., Moe M., Herwig F., Mac Low M.-M., Paxton B., 2011, *MNRAS*, **411**, 2277
- Decin L., et al., 2019, *Nature Astronomy*, **3**, 408
- Dermine T., Izzard R. G., Jorissen A., Van Winckel H., 2013, *A&A*, **551**, A50
- Djurasevic G., 1986, *Ap&SS*, **124**, 5
- Dwarkadas V. V., Chevalier R. A., Blondin J. M., 1996, *ApJ*, **457**, 773
- Eggleton P. P., 1983, *ApJ*, **268**, 368
- Esquivel A., Raga A. C., Cantó J., Rodríguez-González A., López-Cámara D., Velázquez P. F., De Colle F., 2010, *ApJ*, **725**, 1466
- Fadeyev Y. A., 2016, *Astronomy Letters*, **42**, 665
- Gail H.-P., Sedlmayr E., 2013, *Physics and Chemistry of Circumstellar Dust Shells*
- García-Segura G., Langer N., Różyczka M., Franco J., 1999, *ApJ*, **517**, 767
- García-Segura G., Villaver E., Langer N., Yoon S.-C., Manchado A., 2014, *ApJ*, **783**, 74
- García-Segura G., Villaver E., Manchado A., Langer N., Yoon S.-C., 2016, *ApJ*, **823**, 142
- García-Segura G., Ricker P. M., Taam R. E., 2018, *ApJ*, **860**, 19
- Gawryszczak A. J., Mikołajewska J., Różyczka M., 2002, *A&A*, **385**, 205
- Gullikson K., Kraus A., Dodson-Robinson S., 2016, *AJ*, **152**, 40
- Hillwig T. C., Jones D., De Marco O., Bond H. E., Margheim S., Frew D., 2016, *ApJ*, **832**, 125
- Höfner S., Olofsson H., 2018, *A&ARv*, **26**, 1
- Holzer T. E., MacGregor K. B., 1985, in Morris M., Zucker- man B., eds, Vol. 117, *Mass Loss from Red Giants*. p. 229, doi:10.1007/978-94-009-5428-1_21
- Huarte-Espinosa M., Frank A., Balick B., Blackman E. G., De Marco O., Kastner J. H., Sahai R., 2012, *MNRAS*, **424**, 2055
- Iben Jr. I., 2013, *Stellar Evolution Physics, Volume 1: Physical Processes in Stellar Interiors*
- Icke V., Preston H. L., Balick B., 1989, *AJ*, **97**, 462
- Icke V., Balick B., Frank A., 1992, *A&A*, **253**, 224
- Ivanova N., et al., 2013, *A&ARv*, **21**, 59
- Jones D., Mitchell D. L., Lloyd M., Pollacco D., O'Brien T. J., Meaburn J., Vaytet N. M. H., 2012, *MNRAS*, **420**, 2271
- Kahn F. D., West K. A., 1985, *MNRAS*, **212**, 837
- Khouri T., et al., 2014, *A&A*, **570**, A67
- Kwok S., 2000, *The Origin and Evolution of Planetary Nebulae*
- Kwok S., 2002, in Moffat A. F. J., St-Louis N., eds, *Astronomical Society of the Pacific Conference Series Vol. 260, Interacting Winds from Massive Stars*. p. 245
- Kwok S., Purton C. R., Fitzgerald P. M., 1978, *ApJ*, **219**, L125
- Lamers H. J. G. L. M., Cassinelli J. P., 1999, *Introduction to Stellar Winds*
- Lebzelter T., Hinkle K. H., 2002, in Aerts C., Bedding T. R., Christensen-Dalsgaard J., eds, *Astronomical Society of the Pacific Conference Series Vol. 259, IAU Colloq. 185: Radial and Nonradial Pulsations as Probes of Stellar Physics*. p. 556 (arXiv:astro-ph/0202476)
- Leisenring J. M., Kemper F., Sloan G. C., 2008, *ApJ*, **681**, 1557
- Lodders K., Fegley B. J., 1995, *Meteoritics*, **30**, 661
- Manchado A., Guerrero M. A., Stanghellini L., Serra-Ricart M., 1996, *The IAC morphological catalog of northern Galactic planetary nebulae*
- Mastrodemos N., Morris M., 1999, *ApJ*, **523**, 357
- McDonald I., De Beck E., Zijlstra A. A., Lagadec E., 2018, *MNRAS*, **481**, 4984
- Mellema G., Eulderink F., Icke V., 1991, *A&A*, **252**, 718
- Mohamed S., Podsiadlowski P., 2007, in Napiwotzki R., Burleigh M. R., eds, *Astronomical Society of the Pacific Conference Series Vol. 372, 15th European Workshop on White Dwarfs*. p. 397
- Norris B. R. M., et al., 2012, *Nature*, **484**, 220
- Nowotny W., Höfner S., Aringer B., 2010, *A&A*, **514**, A35
- Ohlmann S. T., Röpke F. K., Pakmor R., Springel V., 2016, *ApJ*, **816**, L9
- Ostlie D. A., Cox A. N., 1986, *ApJ*, **311**, 864
- Paczyński B., 1971, *ARA&A*, **9**, 183
- Paczynski B., 1977, *ApJ*, **216**, 822
- Passy J.-C., et al., 2012, *ApJ*, **744**, 52
- Pejcha O., Metzger B. D., Tomida K., 2016, *MNRAS*, **455**, 4351
- Prust L. J., Chang P., 2019, *MNRAS*, **486**, 5809
- Ramstedt S., Schöier F. L., Olofsson H., 2009, *A&A*, **499**, 515
- Rau G., Paladini C., Hron J., Aringer B., Groenewegen M. A. T., Nowotny W., 2015, *A&A*, **583**, A106
- Rau G., Nielsen K. E., Carpenter K. G., Airapetian V., 2018, *ApJ*, **869**, 1
- Renzini A., 1981, in Iben Jr. I., Renzini A., eds, *Astrophysics and Space Science Library Vol. 88, Physical Processes in Red Giants*. pp 431–446, doi:10.1007/978-94-009-8492-9_48
- Ricker P. M., Taam R. E., 2012, *ApJ*, **746**, 74
- Ruffert M., 1993, *A&A*, **280**, 141
- Sabach E., Hillel S., Schreier R., Soker N., 2017, *MNRAS*, **472**, 4361
- Sahai R., Morris M., Sánchez Contreras C., Claussen M., 2007, *AJ*, **134**, 2200
- Sana H., et al., 2012, *Science*, **337**, 444
- Schwarz H. E., Monteiro H., 2004, in Meixner M., Kastner J. H., Balick B., Soker N., eds, *Astronomical Society of the Pacific Conference Series Vol. 313, Asymmetrical Planetary Nebulae III: Winds, Structure and the Thunderbird*. p. 497 (arXiv:astro-ph/0310074)
- Shiber S., Iaconi R., De Marco O., Soker N., 2019, *MNRAS*, **488**, 5615
- Shu F. H., Lubow S. H., Anderson L., 1979, *ApJ*, **229**, 223
- Sloan G. C., et al., 2010, *ApJ*, **719**, 1274
- Soker N., Livio M., 1989, *ApJ*, **339**, 268
- Staff J. E., De Marco O., Macdonald D., Galaviz P., Passy J.-C., Iaconi R., Low M.-M. M., 2016, *MNRAS*, **455**, 3511
- Stanghellini L., Guerrero M. A., Cunha K., Manchado A., Villaver E., 2006, *ApJ*, **651**, 898
- Toledo-Roy J. C., Velázquez P. F., Esquivel A., Giacani E., 2014, *MNRAS*, **437**, 898
- Torres G., Andersen J., Giménez A., 2010, *A&ARv*, **18**, 67
- Townsend R. H. D., 2009, *ApJS*, **181**, 391
- Van Winckel H., Lloyd Evans T., Reyniers M., Deroo P., Gielen C., 2006, *Mem. Soc. Astron. Italiana*, **77**, 943
- Vassiliadis E., Wood P. R., 1993, *ApJ*, **413**, 641
- Wittkowski M., et al., 2018, *A&A*, **613**, L7
- de Val-Borro M., Karovska M., Sasselov D., 2009, *ApJ*, **700**, 1148
- van Belle G. T., Thompson R. R., Creech-Eakman M. J., 2002, *AJ*, **124**, 1706

APPENDIX A: CURVE FITTING

This paper has been typeset from a $\text{\TeX}/\text{\LaTeX}$ file prepared by the author.

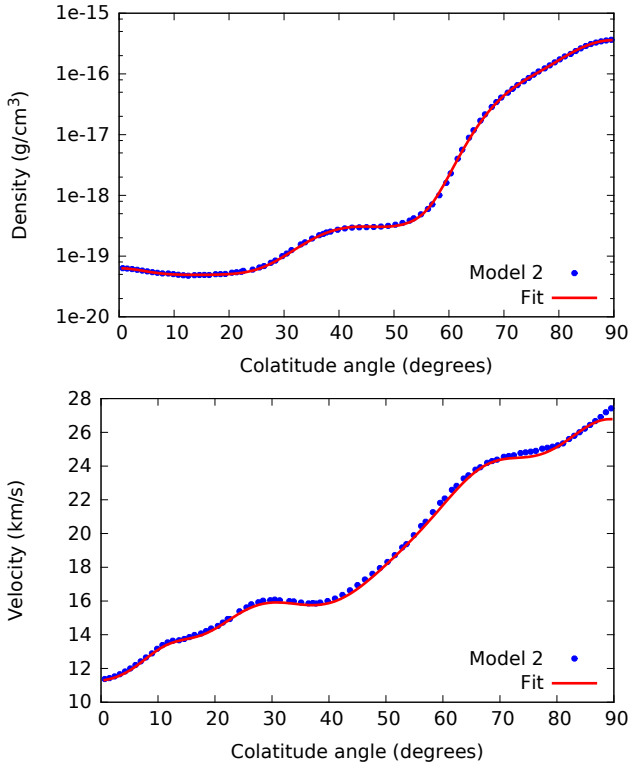


Figure A1. Same as Fig. 11 for model 2.

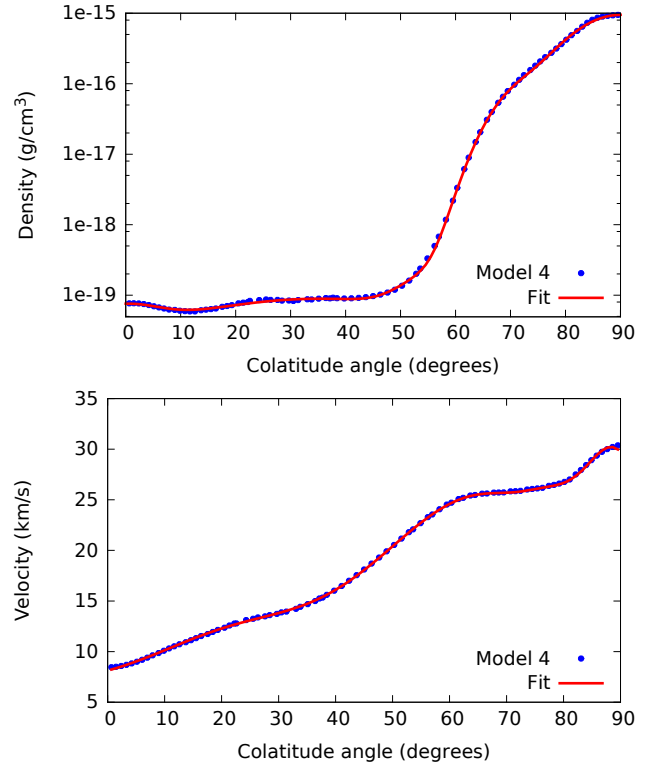


Figure A3. Same as Fig. 11 for model 4.

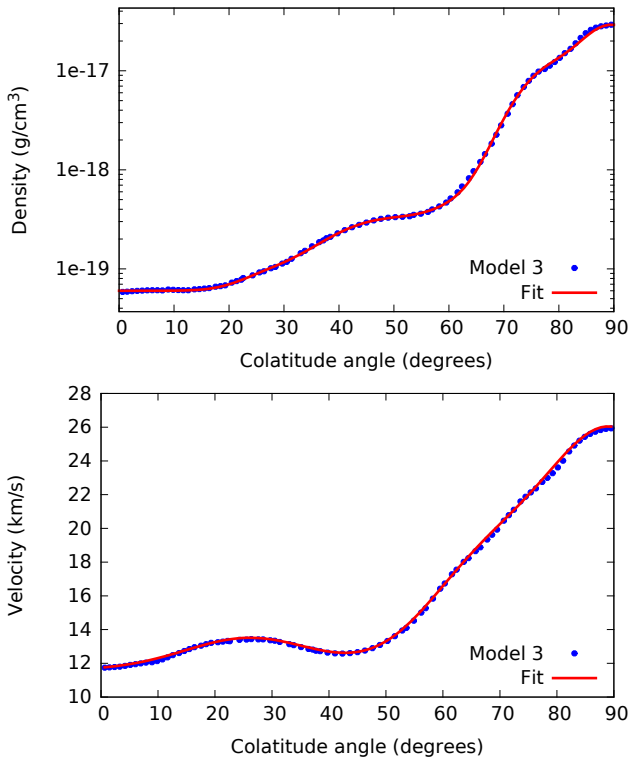


Figure A2. Same as Fig. 11 for model 3.

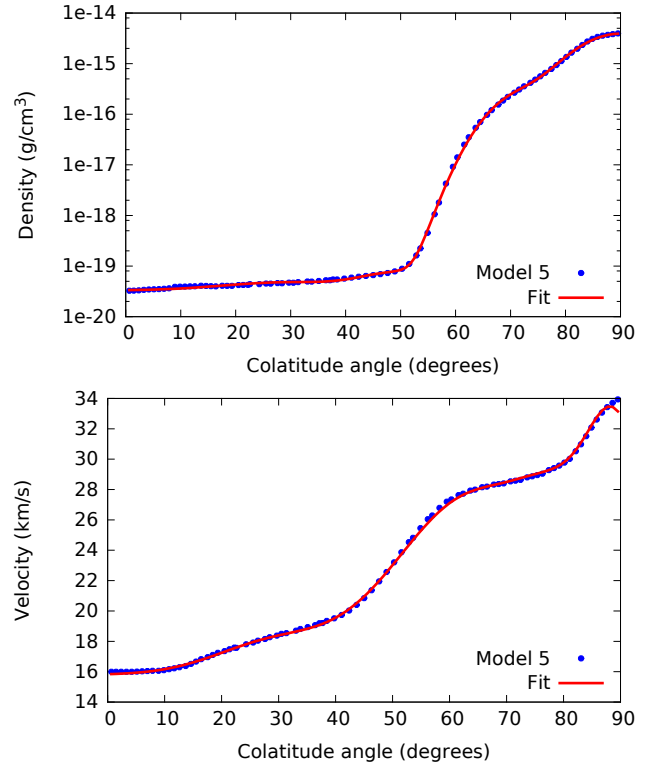


Figure A4. Same as Fig. 11 for model 5.

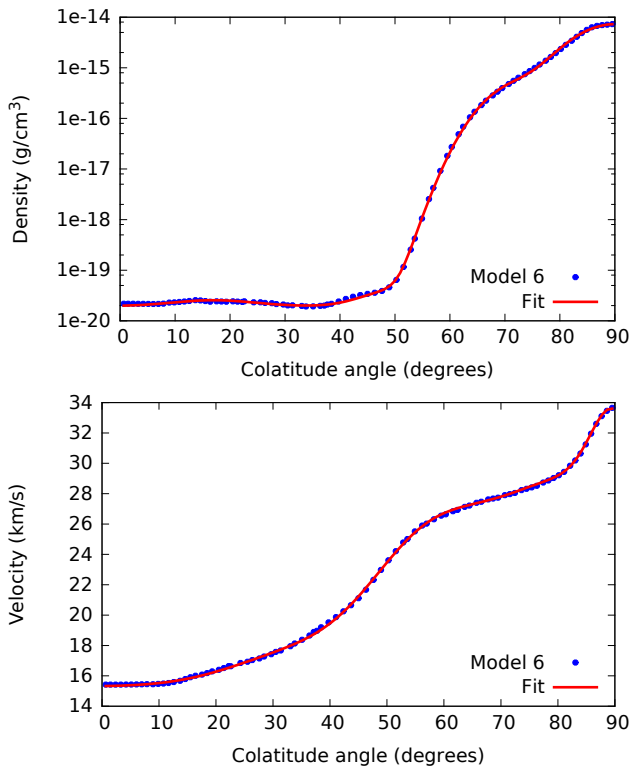


Figure A5. Same as Fig. 11 for model 6.

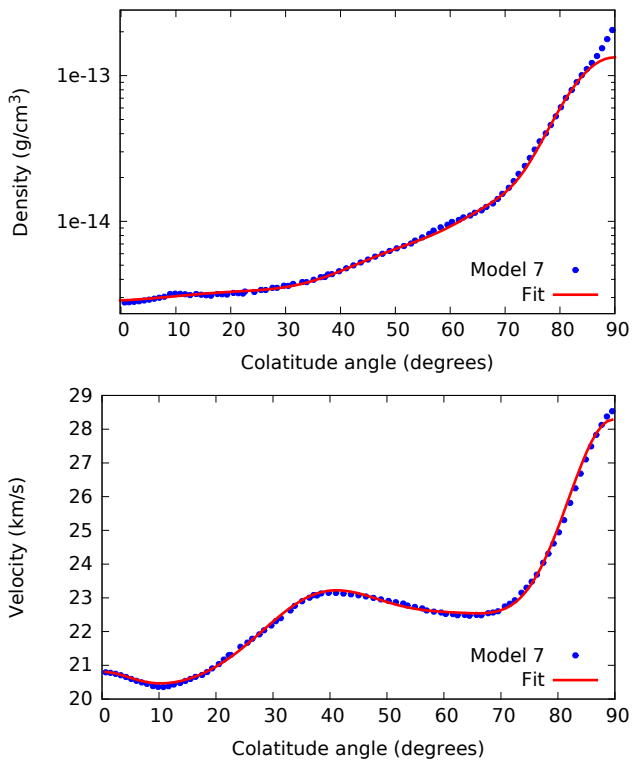


Figure A6. Same as Fig. 11 for model 7.